

La₃Pd₂NaO₉: A High-Valent Insulating Palladate

Qingqing Yang,¹ Ning Guo,² Tiejian Chang,³ Zheng Guo,¹ Xiaoli Wang,¹ Chuanyan Fan,¹ Chao Liu,¹ Lu Han,¹ Feiyu Li,¹ Tao He,¹ Qiang Zheng,² Yu-Sheng Chen,³ Junjie Zhang^{1*}

¹Institute of Crystal Materials, State Key Laboratory of Crystal Materials, Shandong University, Jinan 250100, Shandong, China

²CAS Key Laboratory of Standardization and Measurement for Nanotechnology, CAS Center for Excellence in Nanoscience, National Center for Nanoscience and Technology, Beijing 100190, China

³NSF's ChemMatCARS, The University of Chicago, Argonne, IL 60439, USA

*Email: junjie@sdu.edu.cn

Abstract: A high-valent palladate, La₃Pd₂NaO₉, has been synthesized for the first time. Single crystals with dimensions of 20 μm on edge were successfully grown using the flux method at 420 °C and 70 bar oxygen pressure. Energy dispersive spectroscopy (EDS) and inductively coupled plasma mass spectroscopy (ICP) measurements show that the atomic ratio of La: (Pd+Na) is 3: 3 and Pd: Na is 2: 1. X-ray photoelectron spectroscopy (XPS) measurements show that the oxidation state of Pd is dominated by +4. Synchrotron X-ray single-crystal diffraction measurements revealed that this material crystallizes in the monoclinic *P2₁/c* space group with charge ordering of Na and Pd. Real-space imaging via scanning transmission electron microscopy (STEM) confirmed the crystal structure and revealed excellent sample homogeneity. Electrical resistivity measurements show an insulating behavior. Magnetic measurements show an unexpected paramagnetic behavior, which probably originate from a small fraction of high-spin Pd²⁺ evidenced by XPS. The successful growth of La₃Pd₂NaO₉ single crystals with a high-valent oxidation state of Pd offers an approach for exploring interesting palladates, including potential bilayer Ruddlesden-Popper palladates analogous to the high temperature superconducting La₃Ni₂O₇.

Keywords: high-valent palladate; charge ordering; high pO₂ crystal growth; flux growth; perovskite.

1. Introduction

Since the discovery of cuprate high-temperature superconductors in 1986,¹ clarifying the mechanism of high-temperature superconductivity has been a challenge in the fields of condensed matter physics and materials science.²⁻⁵ One strategy is to look for cuprate analogs to explore more high-temperature superconducting systems.⁶ Ni, which is next to Cu in the periodic table, has attracted a lot of attention.⁷⁻¹³ The report of superconductivity in Nd_{0.8}Sr_{0.2}NiO₂ thin films in 2019 triggered a research boom in nickelate superconductivity,¹⁴ and since then more nickel-based thin film superconductors have been reported.¹⁵⁻¹⁹ These films are obtained by topotactic reduction of corresponding Ruddlesden-Popper (R-P) phases R_{n+1}Ni_nO_{3n+1} (R being a lanthanide). Among them, the material with the highest superconducting transition temperature (*T_c*) is (Sm-Eu-Ca-Sr)NiO₂ with ~ 37 K.¹⁹ In 2023, bulk single crystals of the bilayer R-P phase La₃Ni₂O₇ were reported to show signature of superconductivity with a transition temperature close to 80 K at pressures higher than 14 GPa,²⁰⁻²² making it a potential material for high-temperature superconductivity. Later, the trilayer R₄Ni₃O₁₀ was also reported to superconduct under high pressures.²³⁻²⁷ In addition, bulk nickelates with new crystal structures were designed and synthesized, including hybrid R-P nickelates La₂NiO₄·La₃Ni₂O₇²⁸ and La₂NiO₄·La₄Ni₃O₁₀,²⁹⁻³¹ the former of which has been observed to have a *T_c* ~ 64 K under high pressure.³² Recently, La₃Ni₂O₇ thin films annealed in ozone were also reported to show signature of superconductivity with a *T_c* ~ 45 K at ambient pressure.^{33, 34} More recently, by introducing chemical pressure, Li et al. succeeded in growing high quality single crystals of La₂SmNi₂O₇ at ambient pressure, and pushing the superconducting transition temperature to above 90 K, which is the highest among the nickelate superconductors.³⁵

A natural question is whether there exist superconductors in palladates since Pd is just locating below Ni in the next

periodic row. Palladates have been predicted to be superconductors for a long time.³⁶⁻⁴¹ The oxidation state of palladium in most predicted palladate superconductors is monovalent. Based on theoretical calculations, the Pd⁺-4d orbitals reside between the 3d orbitals of Cu²⁺ and Ni⁺ in the energy level diagrams, and closer to Cu²⁺ compared to Ni⁺.⁴⁰ The larger core charge of Pd strongly attracts electrons, and the larger band-width in Pd⁺-4d lead to stronger hybridization with the 2p orbitals of O²⁻ than Ni⁺-O.⁴⁰ Transition metal and oxygen hybridization is important for high- T_c superconductors,^{6, 42} thus palladates are promising candidates to explore. In real materials, Pd⁺-oxides are very rare. Only PdAO₂ (A = Co, Cr, Rh),⁴³⁻⁴⁵ whose structure is a stacked arrangement of Pd⁺ metallic triangular layers and AO₂ layers, have been reported. Up to date, no palladates with square lattice of Pd⁺ has been synthesized.

A feasible way to prepare Pd⁺-oxides is topotactic reduction of R-P palladates R_{n+1}Pd_nO_{3n+1} (R being a lanthanide), similar to nickelates⁴⁶ and iron oxides.⁴⁷ Along this line, square-lattice LaPdO₂ and La₄Pd₃O₈ has been proposed via reducing LaPdO₃ and La₄Pd₃O₁₀, respectively.³⁶ For R-P palladates, only n = 1 member (R₂PdO₄)⁴⁸ and n = ∞ member (LaPdO₃)⁴⁹ have been synthesized. R₂PdO₄ with T'-structure, the same as Nd₂CuO₄,⁵⁰ has been reported for a variety of lanthanide ions and both polycrystalline samples and thin films (unfortunately no single crystals have been reported up to date) have been synthesized.^{48, 51, 52} These single-layer palladates are insulators and exhibit diamagnetic behavior, consistent with the low spin d⁸ configuration.^{48, 51, 52} The resistivity decreases after electron doping by substituting La³⁺ with Ce⁴⁺, but it still shows semiconducting behavior with temperature.^{51, 52} One exception is the thin film samples annealed in vacuum, where a metal-insulator transition was observed.⁵² For n = ∞, polycrystalline LaPdO₃ with paramagnetic behavior was synthesized under a high pressure of 5 GPa.⁴⁹ The electronic configuration of Pd has been proposed to be t_{2g}⁶σ^{*1}, which should exhibit metallic behavior. Later, Penny G⁵³ measured the resistivity of high-pressure synthesized LaPdO₃ pellet containing KCl and impurities such as La₂Pd₂O₅ and PdO, and they claimed that LaPdO₃ is metallic due to its low resistivity (< 0.1 Ω cm below 350 K) although a small increase of resistivity with decreasing temperature is seen. No other R-P palladates have been reported up to date due to the dominance of La₄PdO₇ and La₂Pd₂O₅ in the thermodynamic phase diagram.⁵⁴

In this contribution, we attempted to grow LaPdO₃ crystals using NaOH-KOH flux at pO₂ = 70 bar and T = 420 °C for subsequent topotactic reduction to obtain LaPdO₂. Unexpectedly, 1/3 of the Pd site was substituted by Na, resulting in a high valence palladate, La₃Pd₂NaO₉, evidenced by EDS, ICP and XPS data. XPS measurement shows that the oxidation state of Pd is dominated by +4 with a small amount of +2. Real-space imaging via STEM revealed a perovskite-like structure and excellent sample homogeneity. Synchrotron X-ray single-crystal diffraction determined that the material crystallizes in the monoclinic *P*2₁/*c* space group with charge ordering of Na and Pd. Resistivity measurements show that La₃Pd₂NaO₉ is an insulator, which is consistent with charge ordering of Na and Pd. The magnetization data show an anomalous paramagnetic behavior, which can be attributed to the presence of a small fraction of high-spin Pd²⁺ as evidenced by XPS. The successful preparation of La₃Pd₂NaO₉ opens a door for preparing single crystals of other interesting palladates, including potential bilayer R-P palladates analogous to the high temperature superconducting La₃Ni₂O₇.

2. Experimental Section

2.1 High pO₂ Flux Growth of La₃Pd₂NaO₉ Crystals. All experiments were carried out at a high-pressure flux furnace designed for operation at $T_{\max} = 500$ °C and $P_{\max} = 160$ bar (Xi'an Taikang Biotechnology Co., Ltd). La₂O₃ (Sigma Aldrich, 99.99%), Pd (Aladdin, 99.5%), NaOH (Aladdin, 99.9%) and KOH (Aladdin, 99.99%) were used as raw materials. La₂O₃ was baked at 650 °C for 10 h before use. Powders of La₂O₃ and Pd with a stoichiometric ratio were weighed, mixed, and ground and then it was mixed with NaOH-KOH (molar ratio 1:1) flux in a glove box at a weight ratio of 1:5, 1:10, or 1:20 (see **Table S1**). The mixture was placed in an Al₂O₃ crucible (Φ30 mm × 30 mm), which was then covered with a flat lid and put into the high-pressure furnace. The furnace was purged with high-purity oxygen several times. Afterwards, certain amount of high-purity oxygen was filled into the furnace at room

temperature, so that when the furnace temperature reached 420 °C, the target pO₂ (e.g., 10, 30, 50, or 70 bar) was achieved inside the furnace. The furnace was maintained at targeted temperature and pO₂ for 48 h in order to dissolve raw materials. During this period, oxygen is consumed due to the reaction of raw materials to form La₃Pd₂NaO₉. Therefore, we connected the gas inlet to the oxygen cylinder and adjusted it through a pressure regulator to maintain the pressure at the expected value. After dwelling, the furnace was cooled down to 300 °C at the rate of 3.5, 3, 2.5, or 2 °C/h, followed by furnace cooling to room temperature. Finally, the remaining flux was removed with distilled water and black crystals with shiny facets were obtained.

2.2 Powder X-ray Diffraction (PXRD). A Bruker AXS D2 Phaser X-ray powder diffractometer was used to check phase purity. Data were collected at room temperature using Cu K_α radiation ($\lambda = 1.5418 \text{ \AA}$) in the 2θ range of 10-100° with a scan step size of 0.02° and a scan time of 0.5 s per step. TOPAS 6 was used for Rietveld refinement. Refinement parameters include the background (Chebychev function, order 11), zero shift, lattice parameters, crystallite size L, strain G, atomic positions, and thermal parameters.

2.3 Scanning Electron Microscopy (SEM). The morphology of the as-grown crystals was observed using a scanning electron microscope. The SEM images were obtained by a Zeiss Gemini SEM 500 microscope incident electron of 3.00 KV.

2.4 EDS. The Oxford UltimMax 170 energy spectrum on Zeiss Gemini SEM 500 was used for qualitative and quantitative analyses of the as-grown crystals.

2.5 ICP. The Inductively Coupled Plasma Mass Spectrometer PerkinElmer-Avio550 max was used for quantitative analysis of crystals. Crystals of 4.6 mg were thoroughly ground and dissolved in 5 mL of concentrated nitric acid (GR). The samples of 350, 500, 500, 800, and 800 μL were taken using a pipette gun and poured into a 100 mL volumetric flask. Distilled water was added to dilute and shake well. 10 mL of solution was taken from each volumetric flask as samples 1-5 for measurements. Blank was also prepared to ensure the accuracy of the test. 350, 500, 500, 800, and 800 μL nitric acid (GR) were taken using a pipette gun and poured into a 100 mL volumetric flask. Distilled water was added to dilute and shake well. 10 ml of solution was taken from each volumetric flask as blank samples 1-5 for measurements. The final concentration of each element tested was determined by subtracting the data of blank samples 1-5 from the data of samples 1-5.

2.6 XPS. The crystals were ground and pressed into a smooth, flat pellet for measurement. The oxidation state of Pd was measured using a PHI Genesis 500 X-ray photoelectron spectrometer with an Al K_α light source, a spot diameter of 200 μm , and a fine scan was performed in the range of 330-350 eV. The software Avantage was used to process the XPS measurement data.

2.7 Synchrotron X-ray Single-Crystal Diffraction (SXRD). SXRD data were collected using synchrotron radiation ($\lambda = 0.43060 \text{ \AA}$) at GeoSoilEnviroCARS (Sector 13) at the Advanced Photon Source, Argonne National Laboratory. A single crystal with dimension of $\sim 15 \mu\text{m}$ was mounted to the tip of glass fiber and measured using a Huber 3-circle diffractometer. Indexing, data reduction, and image processing were performed using Bruker APEX5 software.⁵⁵ The structure was solved by direct methods and refined with full matrix least-squares methods on F^2 . All atoms were modeled using anisotropic ADPs, and the refinements converged for $I > 2\sigma(I)$, where I is the intensity of reflections and $\sigma(I)$ is the standard deviation. Calculations were performed using the SHELXTL crystallographic software package.⁵⁵ Details of crystal parameters, data collection, and structure refinement at 296(2) K are summarized in **Table 1**, and atomic coordinates and equivalent isotropic atomic displacement parameters are listed in **Table 2**. Further details of the crystal structure investigations may be obtained from the joint CCDC/FIZ Karlsruhe online deposition

service by quoting the deposition number CSD 2445228.

Table 1. Crystal data and structure refinement for La₃Pd₂NaO₉.

Empirical formula	La ₃ Pd ₂ NaO ₉
Formula weight	796.73
Temperature	296(2) K
Crystal system	Monoclinic
Space group	P2 ₁ /c
<i>a</i>	16.777(5) Å
<i>b</i>	5.8311(17) Å
<i>c</i>	9.759(3) Å
α	90°
β	124.969(3)°
γ	90°
Cell volume	782.3(4) Å ³
<i>Z</i>	4
Calculated density	6.765 g/cm ³
μ	11.147 mm ⁻¹
F (000)	1384.0
Radiation	synchrotron X-ray ($\lambda = 0.43106$ Å)
2 θ range for data collection	1.796 to 46.136°
Index ranges	-29 $\leq h \leq$ 29, -9 $\leq k \leq$ 9, -14 $\leq l \leq$ 14
Reflections collected	10532
Independent reflections	3448 [R _{int} = 0.0678, R _{sigma} = 0.1802]
Data/restraints/parameters	3448/0/144
Goodness-of-fit on F ²	0.902
Final R indexes [I \geq 2 σ (I)]	R ₁ = 0.0575, wR ₂ = 0.1847
Final R indexes [all data]	R ₁ = 0.0756, wR ₂ = 0.2145
Largest diff. peak/hole	3.50/-3.27 e Å ⁻³

Table 2. Atomic coordinates occupancy and thermal vibration parameters of La₃Pd₂NaO₉.

Site	Atom	<i>x</i>	<i>y</i>	<i>z</i>	Occ	U _{eq}
La1	La	0.92472(3)	0.56136(7)	0.25262(6)	1	0.00718(18)
La2	La	0.74468(3)	0.44213(7)	0.74862(5)	1	0.00726(18)
La3	La	0.41598(3)	0.43997(7)	-0.24597(5)	1	0.00760(18)
Pd1	Pd	0.67075(4)	0.50300(7)	0.00528(7)	0.879(6)	0.0049(2)
Pd2	Pd	0.82989(3)	0.49798(7)	0.49847(7)	0.872(6)	0.0048(2)
Pd3	Pd	1	0.5	1	0.265(7)	0.0070(7)
Pd4	Pd	0.5	0.5	-0.5	0.237(7)	0.0059(7)
Na1	Na	0.67075(4)	0.50300(7)	0.00528(7)	0.121(6)	0.0049(2)
Na2	Na	0.82989(3)	0.49798(7)	0.49847(7)	0.128(6)	0.0048(2)
Na3	Na	1	0.5	1	0.735(7)	0.0070(7)
Na4	Na	0.5	0.5	-0.5	0.763(7)	0.0059(7)
O1	O	0.7514(4)	0.7985(8)	0.4482(7)	1	0.0103(10)

O2	O	0.7131(4)	0.3001(8)	0.4481(7)	1	0.0106(9)
O3	O	0.5877(4)	0.3098(9)	0.0478(7)	1	0.0140(10)
O4	O	0.9098(4)	0.2116(9)	0.5478(7)	1	0.0138(10)
O5	O	0.9434(4)	0.6901(9)	0.5457(7)	1	0.0134(10)
O6	O	0.6211(4)	0.7834(9)	0.0486(7)	1	0.0128(10)
O7	O	0.5592(4)	0.5259(9)	-0.2389(8)	1	0.0150(11)
O8	O	0.7854(4)	0.4703(8)	0.2525(8)	1	0.0117(10)
O9	O	0.8823(4)	0.5258(9)	0.7385(8)	1	0.0118(10)

2.8 STEM. The single crystals were crushed in ethanol, and drops of the suspensions were deposited on lacey carbon-coated molybdenum grids and dried in air for STEM observations. High-angle annular dark-field (HAADF)-STEM images were obtained at an accelerating voltage of 300 kV on an aberration-corrected transmission electron microscope (Spectra 300, Thermo Fisher Scientific), equipped with a field-emission electron gun. The probe convergence semi-angle and inner collection semi-angle are 25.0 mrad and 49.0 mrad, respectively.

2.9 Resistivity. The resistivity of $\text{La}_3\text{Pd}_2\text{NaO}_9$ was measured by the standard four-probe method. The crystals were too small to make four contacts, thus, we ground the crystals into powder and pressed them into a pellet. Then, the pellet was cut into two parts, one part for resistivity measurement and the other part was annealed in the high-pressure furnace at 420 °C and 70 bar O_2 for 3 days. The densities of the pellets before and after annealing were about 65% and 73% of single crystals, respectively. The pellet was cut into long and thin bars for making electrodes with DuPont silver paste. Resistivity was measured in the range of 160-300 K (four-probe method) and 100-300 K (two-probe method) on warming at a rate of 2 K/min on a Quantum Design magnetic property measurement system (MPMS3) with Electrical Transport Option without external magnetic field.

2.10 Magnetic Susceptibility. Magnetic susceptibility of the samples was measured using a Quantum Design MPMS3 VSM. Crystals of 32.8 mg were ground into powders and pressed into a pellet, and then glued onto the quartz rod using GE varnish. ZFC-W (zero-field cooling and data collected on warming), FC-C (field cooling and data collected on cooling), and FC-W (field cooling and data collected on warming) data were collected between 1.8 and 300 K under an external magnetic field of 1 T. The sample was cooled to 10 K at a rate of 10 K/min in zero field and held at 10 K for 10 min and then cooled to 1.8 K at a rate of 2 K/min and held at 1.8 K for 10 min. Then, we applied magnetic field to 1 T and magnetic susceptibility was recorded on warming (3 K/min). In the FC-C and FC-W procedures, the magnetic susceptibility was also recorded (3 K/min) in a fixed field of 1 T. Magnetization data as a function of the magnetic field were collected between -7 to $+7$ T with a sweep mode of 300 Oe/s at 1.8, 150, and 300 K. For comparison, the as-grown single crystals were also measured to explore if sodium in the material absorbs moisture that might result in different magnetic properties.

3. Results and Discussion

3.1 High $p\text{O}_2$ Synthesis and Crystal Growth. We have been exploring the possibility to synthesize R-P palladates with $n > 1$ at ambient pressure using the flux method. Initially, we tried the carbonate fluxes, hydroxide fluxes and chloride fluxes because R-P nickelates were synthesized using such fluxes;⁵⁶⁻⁶¹ however, we did not obtain any palladates with palladium valence of larger than +2 (see **Table S2** and **Figures S1-S5**). The failure to obtain high-valence Pd is probably due to insufficient oxidization; flux growth under high oxygen pressure may work. Among the above-mentioned fluxes, the melting points of carbonates are high (850 °C for Na_2CO_3 and 890 °C for K_2CO_3). In contrast, chlorides are corrosive at high oxygen pressure and it's very difficult to find a suitable crucible (Pt and Al_2O_3 did not work) and chamber. Molten alkali hydroxides have been utilized as fluxes for the growth of oxide crystals of the platinum group metals (Ru, Os, Ir, Rh, Pd, Pt) containing lanthanide metal.⁶² It has been reported that divalent

palladium oxides were synthesized using NaOH or KOH flux under normal pressure.⁶³⁻⁶⁵ We expected to synthesize palladium oxides with higher oxidation states under high pO_2 conditions. Among hydroxide fluxes, we started with the NaOH-KOH (molar ratio 1:1) system because it has a lower melting point of ~ 170 °C, and single crystals of NdNiO₃ were successfully grown by our group.⁶⁶

In our initial exploration, La₂O₃ and Pd were mixed according to the molar ratio 1:2, and then it was mixed with flux at a weight ratio of 1:20. The high-pressure furnace was kept at a temperature of 400, 410, or 420 °C under a pO_2 of 10, 30, 50, or 70 bar for 24 or 40 hours, and then cooled down to 300 °C at a rate of 10 °C/h (see specific growth conditions in **Table S1**). XRD analysis revealed the formation of perovskite phase at a pO_2 of ≥ 50 bar and a dwelling temperature of 420 °C (**Figure S6**). However, the positions of the XRD peaks are apparently shifted compared with the peaks of LaPdO₃ in the database (PDF #04-012-7471), indicating changes of lattice parameters. We then optimized the growth conditions, including weight ratio of raw materials to fluxes, dwelling time, and cooling rate in order to obtain pure phase. At a 1:10 weight ratio of raw materials to fluxes, dwelling temperature of 420 °C for 48 h, and a cooling rate of 3.5 °C/h, black powders with tiny but shiny crystals of ~ 5 μm were obtained. We also noticed several weak peaks at 2θ angles smaller than 20° (**Figure S7**) that cannot be indexed using the perovskite structure of LaPdO₃. We performed LeBail fit (**Figure S8**) on the XRD of the crystals, and the results showed remarkable changes in the lattice parameters compared to LaPdO₃.⁴⁹ These results suggest that the as-grown single crystals are probably not LaPdO₃.

We continued to optimize the dwelling time and cooling rate in order to improve the dimensions and quality of crystals. The experimental details are shown in **Table S1**, and the XRD patterns are shown in **Figure S9**. No increase in the size of the crystals was found by extending the dwelling time from 48 h to 60 h. Thus, we used 48 h as the optimal dwelling time. We further slowed down the cooling rate to 2 °C/h, and finally obtained shiny crystals with dimensions of ~ 20 μm on edge (**Figure 1**). Unfortunately, the issue of crucible corrosion was much worse using slower cooling rates and long growth time, preventing us from growing larger single crystals.

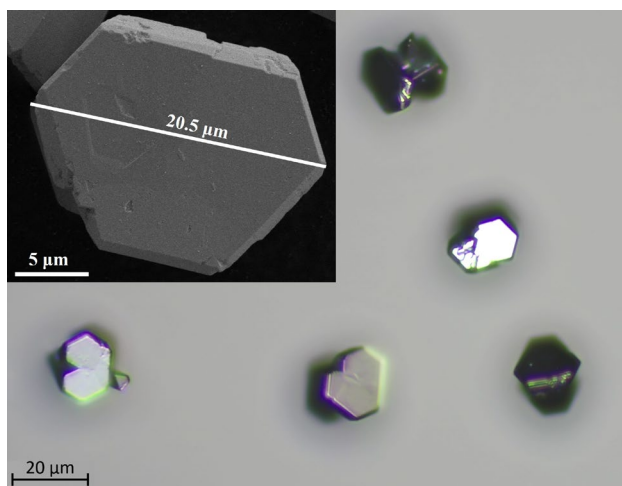


Figure 1. A typical photo of as-grown single crystals using a microscope. Inset shows a scanning electron microscope image.

3.2 Determination of composition. In order to determine the composition and find out the underlying mechanism of the big changes in the lattice parameters compared with perovskite LaPdO₃,⁴⁹ we performed EDS and ICP measurements. For EDS measurements, we selected all possible elements in our raw materials including La, Pd, O, Na, K and Al. We found no Al in the crystals although we used Al₂O₃ crucibles, and we found the presence of a significant amount of Na. **Table S3** lists the EDS data and **Figure S10** presents the raw data. To facilitate the analysis of the data, we normalized the La Atomic% to 1 and averaged the four sets of data. We found that the atomic ratio of La: (Pd+Na) is approximately 3: 3 and Pd: Na is 2: 1. Thus, the chemical formula of the crystal can be expressed as La₃Pd₂NaO_x,

where $\sim 1/3$ of Na substitutes Pd compared to LaPdO_3 . Considering that EDS only measures the surface with several μm in depth, we also measured the La, Pd and Na elements in the crystals by dissolving the crystals into acid using ICP-MS (see **Table S4**), which is an accurate method for determining the concentration of the elements in the bulk form. Five sets of samples containing three different concentrations were measured. Like the analysis of the EDS data, the molar concentration of La was normalized to 1 $\mu\text{mol/L}$ and the five sets of data were averaged. The results are in excellent agreement with the EDS.

3.3 XPS analysis. We carried out XPS measurements to determine the valence of Pd. We first performed a full spectrum scan, and the results are shown in **Figure S11**. Clearly, no Al and K were found. Characteristic peaks from La, Pd, Na, and O are seen, which is in agreement with the EDS and ICP results. Scans near the C1s (280-290 eV) and the Pd3d (330-350 eV) binding energy regions were performed to obtain higher resolution spectrograms. Binding energy values were calibrated using the 284.8 eV peak of C1s . **Figure 2** shows the XPS spectrum of the Pd3d core level. As can be seen, the Pd3d spectrum shows a doublet $\text{Pd3d}_{5/2}$ and $\text{Pd3d}_{3/2}$ separated by 5.22-5.26 eV, in agreement with previous studies.⁶⁷ The two peaks of $\text{Pd3d}_{5/2}$ are located at 337.00 eV and 338.95 eV, respectively. The binding energies were reported to be about 336.1-337.1 eV for Pd^{2+} and 337.7-339.3 eV for Pd^{4+} .⁶⁷⁻⁷⁰ Thus, the peak at 337.00 eV indicates Pd^{2+} , while the peak at 338.95 eV corresponds to Pd^{4+} . The ratio of peak area of $3d_{5/2}$ to $3d_{3/2}$ for Pd^{4+} is 1.63, and 1.52 for Pd^{2+} ; both of them are consistent with the theoretical ratio of 3: 2. The ratio of peak area for Pd^{4+} equal to 77%, indicating that the predominant oxidation state of Pd in the sample is +4, which aligns with our expectations. The presence of Pd^{2+} suggests that our sample does not conform strictly to stoichiometry, possibly due to the existence of oxygen vacancies. Based on the amount of Pd^{4+} (77%) and Pd^{2+} (23%), and the atomic ratio of $\text{La/Pd/Na}=3:2:1$ from EDS and ICP, the oxygen content is estimated to be 8.55. Therefore, we estimate the chemical formula of the as-grown crystals to be $\text{La}_3\text{Pd}_2\text{NaO}_{8.55}$, which contains 5% oxygen deficiencies from stoichiometry ($\text{La}_3\text{Pd}_2\text{NaO}_9$).

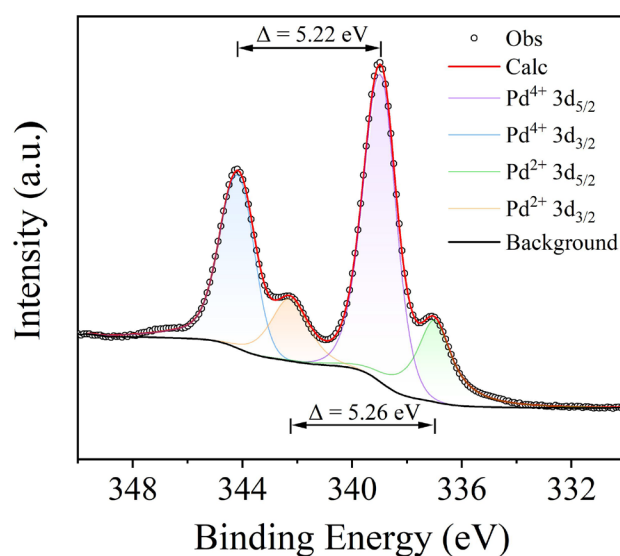


Figure 2. The XPS spectrum of the Pd-3d core level.

3.4 Structural determination. The X-ray powder diffraction pattern matches with a perovskite structure except several peaks at low angles, indicating that the crystal structure is perovskite or distorted perovskite. In principle, single-crystal X-ray diffraction is the best way to determine crystal structure; however, the as-grown crystals are too small, no good diffraction data were obtained via in-house X-ray single crystal diffraction. We thus performed Rietveld refinement on the in-house X-ray powder diffraction data by replacing $1/3$ of Pd in the structural model of LaPdO_3 (space group $Pbnm$).⁴⁹ To ensure the accuracy of the refinement, we only refined a joint thermal parameter. The refinement (see **Figure S12**) converged to $R_{\text{wp}} = 9.86\%$, $R_{\text{exp}} = 5.18\%$, and $\text{GOF} = 1.90$ with lattice parameters of $a =$

5.5729(2) Å, $b = 5.8086(2)$ Å and $c = 7.9657(2)$ Å. Apparently, several diffraction peaks at $2\theta < 20^\circ$ are not accounted by this disordered model. There are two possibilities: (1) These peaks, consistently appeared under different experimental conditions (**Figures S7 and S9**), are intrinsic to our as-grown single crystals. The single crystals are black and the morphologies observed using a microscope are pretty homogeneous, indicating probably a single phase. Along this line, the appearance of these weak peaks at low angles suggests a supercell compared to perovskite cell. (2) These weak peaks belong to impurities. We performed search-match using the latest powder diffraction database [ICDD-PDF-5+ (2025)], but found no match.

To determine the crystal structure, we carried out synchrotron X-ray single crystal diffraction at Beamline 13 at the Advanced Photon Source, Argonne National Laboratory. **Figure 3** shows the reconstructed $(h0l)$ planes based on the perovskite unit cell of $a \sim 5.6$ Å, $b \sim 5.8$ Å and $c \sim 8.0$ Å. Notably, reflection peaks locating at $\mathbf{q} = (1/3, 0, 1/3)$ are clearly seen, indicating that the unit cell should be nine times large. In contrast, no superlattice diffraction peaks are observed on the $(0kl)$ or $(hk0)$ planes (**Figure S13**), possibly because they are too weak. The presence of the superlattice peaks suggests that Na atoms in the crystal likely form an ordered pattern with Pd. We then attempted to solve the crystal structure using the nine-times large supercell; however, we failed due to insufficient data.

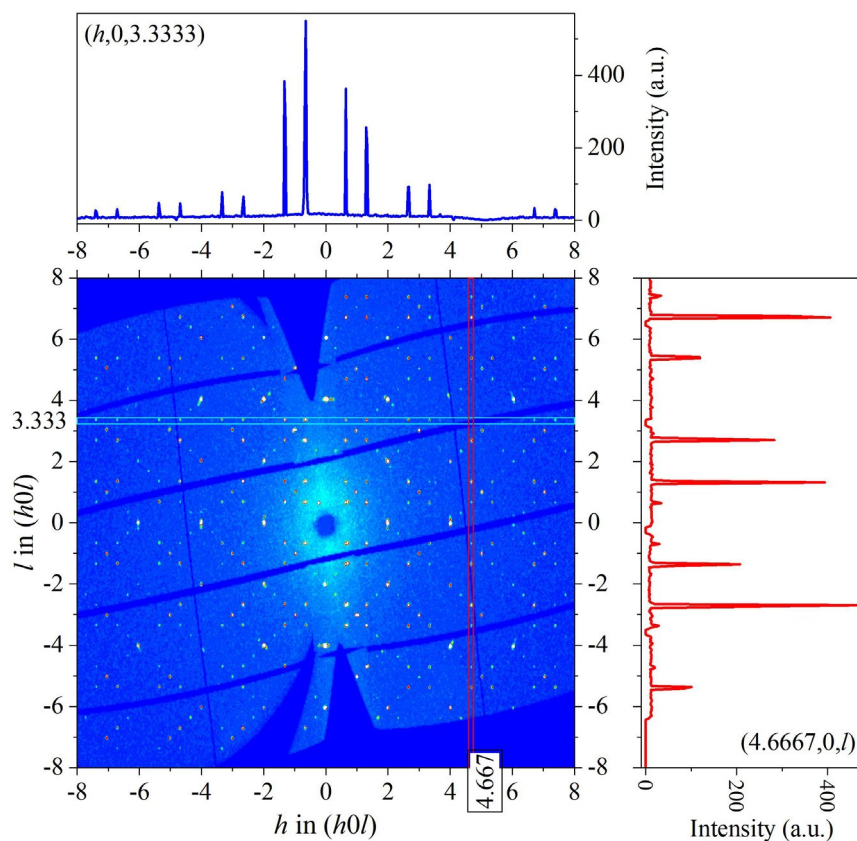


Figure 3. The reconstructed $(h0l)$ planes based on the perovskite unit cell of $a \sim 5.6$ Å, $b \sim 5.8$ Å and $c \sim 8.0$ Å.

By lowering the symmetry to monoclinic $P2_1/c$, we succeeded in solving the crystal structure with lattice parameters of $a = 16.777(5)$ Å, $b = 5.8311(17)$ Å, $c = 9.759(3)$ Å, and $\beta = 124.969(3)^\circ$. Details of the crystal parameters and structure refinement are summarized in **Tables 1 and 2**. As shown in **Figure 4(a-c)**, the structure is a distorted perovskite. The asymmetric unit contains three La atoms, four Pd/Na positions and nine oxygen atoms (see **Table 2**). All Pd/Na atoms are coordinated by six oxygen atoms with bond length ranging from 1.981(6)-2.204(6) Å, forming octahedral environment, as shown in **Figure 4(d)**. These octahedra, where the Pd/Na atoms deviate from the center, share corners with each other. During the refinement process, we observed that some degree of Na disorder persists. However, Na preferentially occupies the Pd3 and Pd4 sites (see **Table 2**), demonstrating an overall charge-ordered state. We used the

average Pd-O and La-O bond lengths, which are La-O = 2.589 Å, Pd(1)-O = 2.044 Å, Pd(2)-O = 2.041 Å, Pd(3)-O = 2.187 Å, Pd(4)-O = 2.183 Å, to estimate the tolerance factor. The Pd(1) and Pd(2) sites are primarily occupied by Pd, while the Pd(3) and Pd(4) sites are mainly occupied by Na. Therefore, the tolerance factor is calculated to be 0.90 based on the average bond lengths of Pd(1)-O and Pd(2)-O, and 0.84 based on the average bond lengths of Pd(3)-O and Pd(4)-O. The tolerance factor in LaPdO₃ is calculated to be 0.87. We note that the tolerance factor for the sites primarily occupied by Pd is slightly larger than that of LaPdO₃, while the tolerance factor for the sites primarily occupied by Na is smaller than that of LaPdO₃. However, all of them significantly deviate from 1, which is consistent with our results that the material is difficult to synthesize at ambient pressure and high oxygen pressure is needed. As shown in **Figure 4(e)**, within the (*h0l*) plane, along the *a*-axis direction, Pd and Na atoms essentially exhibit an ordered arrangement of two Pd layers followed by one Na layer. **Figure 4(f)** compares the unit cells of perovskite (black line rectangle), 3×3 supercell of the perovskite structure (dash rectangle) and our monoclinic *P2₁/c* model (blue parallelogram). We have attempted to topotactically reduce our as-grown sample using CaH₂, and we failed. Now this can be easily understood because of the incorporation of Na in the crystal structure. Along this line, we are exploring other fluxes to grow LaPdO₃ without Na substitution.

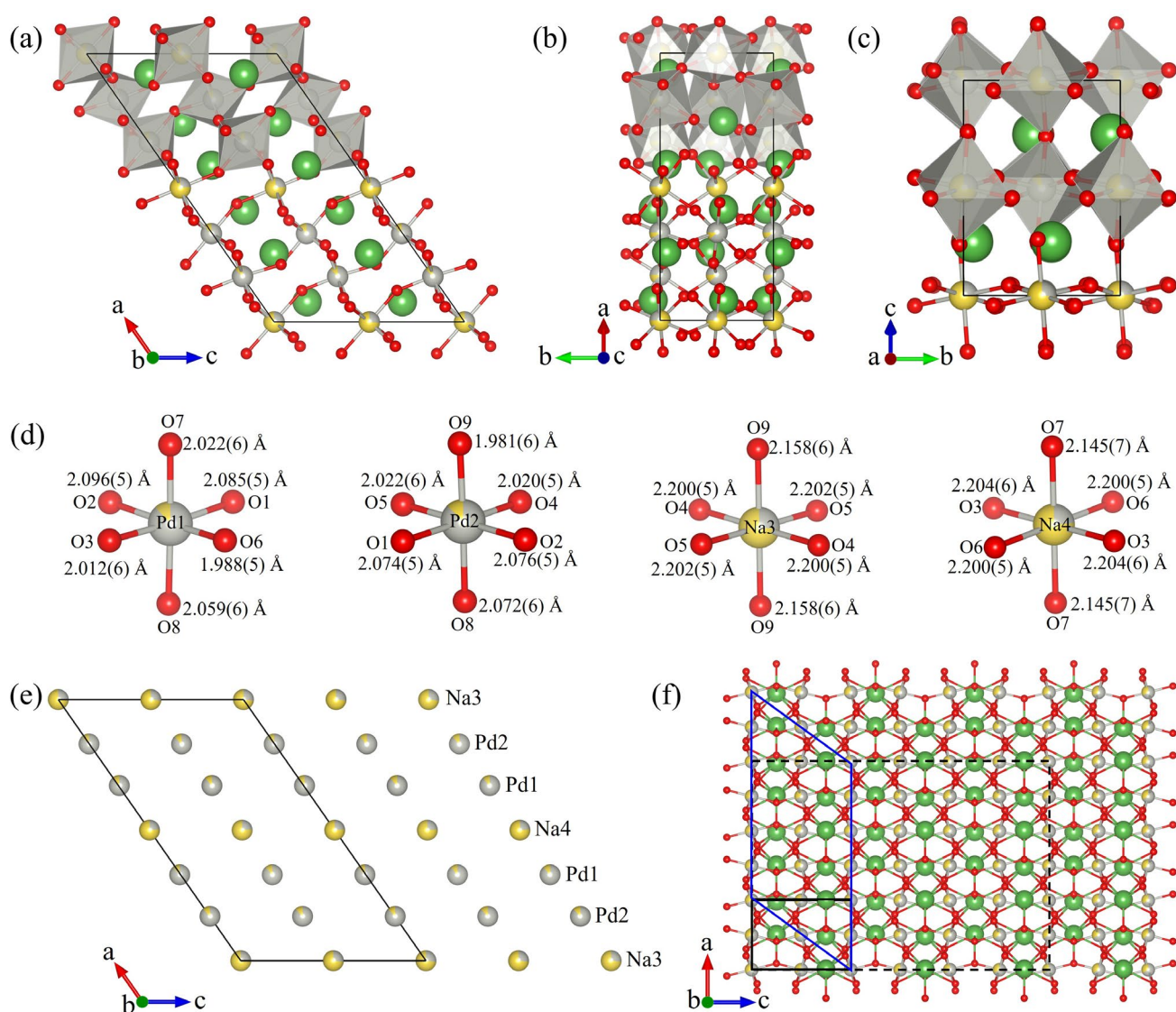


Figure 4. Crystal structure. The gray spheres represent palladium atoms, the yellow spheres represent sodium atoms, the red spheres represent oxygen atoms, the green spheres represent lanthanum atoms. (a-c) Monoclinic *P2₁/c* model obtained by SXRD. Note the model is shown in half polyhedral and half ball-and-stick style. (d) Pd/Na-O octahedral environments with bond lengths labeled of the monoclinic *P2₁/c* model. (e) Charge ordering of Na and Pd. Na and Pd

are disordered, and the dominant one is labeled. (f) The unit cells of perovskite structure of Na disordered occupancy obtained by Rietveld refinement on PXRD (black line rectangle), 3×3 supercell of the perovskite structure (dash rectangle) and monoclinic $P2_1/c$ model (blue parallelogram).

Figure 5 shows the powder diffraction data (**experiment 13** shown in **Table S1**) as well as Rietveld refinement using the single crystal structural model obtained from SXRD (see **Figure S14** for zoom-in of low-angle data $2\theta = 12-25^\circ$ and high-angle data $2\theta = 80-100^\circ$). The refinement converged to $R_{wp} = 8.52\%$, $R_{exp} = 5.18\%$, and GOF = 1.64 with lattice parameters of $a = 16.7184(4) \text{ \AA}$, $b = 5.80857(13) \text{ \AA}$, $c = 9.7216(11) \text{ \AA}$, and $\beta = 124.975(10)^\circ$. It can be clearly seen that all peaks (particularly the low-angle peaks) were well fitted, confirming the single-crystal structure model. To explore whether the content of Na substitution for Pd would be different under different experimental conditions, we also performed Rietveld refinements on the powder diffraction data of the products from **experiments 4, 9, and 10** shown in **Table S1** and list the results in **Table S5**. Powder diffraction data and Rietveld refinement are shown in **Figure S15**. The lattice parameters obtained were basically the same (**Table S5**), indicating that the growth results are consistent and the material is a line compound.

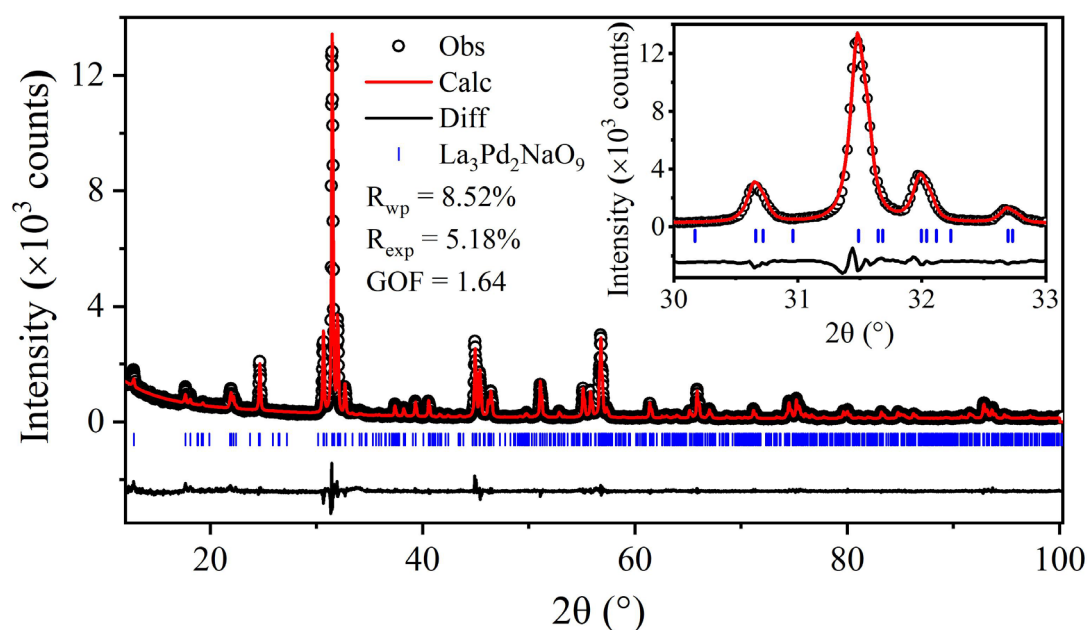


Figure 5. PXRD and Rietveld refinement using the single crystal structural model obtained by SXRD data. Obs: observed intensity; Calc: calculated intensity; Diff: difference.

3.5 STEM analysis. We investigated the local structure of $\text{La}_3\text{Pd}_2\text{NaO}_9$ single crystals using scanning transmission electron microscopy (STEM). Typical high-angle annular dark-field (HAADF)-STEM images along the $[130]$ and $[103]$ projections are shown in **Figure 6** (see **Figure S16** and **S17** for wide range images). The $\text{La}_3\text{Pd}_2\text{NaO}_9$ single crystals exhibits a nice ordered alternating stacking of La-O and Pd/Na-O layers on the scale of tens of nanometers, which is consistent with the single crystal structure and indicates excellent sample homogeneity.

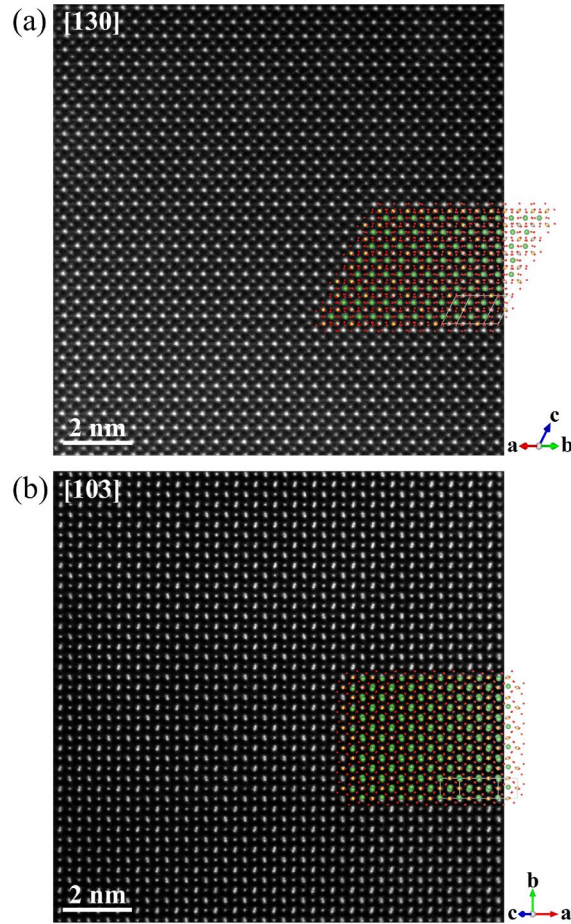


Figure 6. Typical atomic-scale HAADF-STEM images with overlaid single crystal structural model of $\text{La}_3\text{Pd}_2\text{NaO}_9$. (a) along the [130] projection. (b) along the [103] projection.

3.6 Electrical resistivity. Our as-grown crystals are too small to put four leads on, thus we pulverized the crystals to polycrystalline powders and pressed into pellets for electrical resistance measurements. **Figure 7** shows the resistivity as a function of temperature under zero magnetic field, we observed a semiconducting behavior. The as-grown sample shows variable range hopping (VRH) transport at low temperature expressed by $\rho \propto \exp[(\frac{T_0}{T})^{1/(d+1)}]$, where d is the dimension of the system.⁷¹ The good linear fit of the low temperature data at $d = 3$ indicates that the sample charge conducts in three dimensions, consistent with the type of transport in the three-dimensional structure.

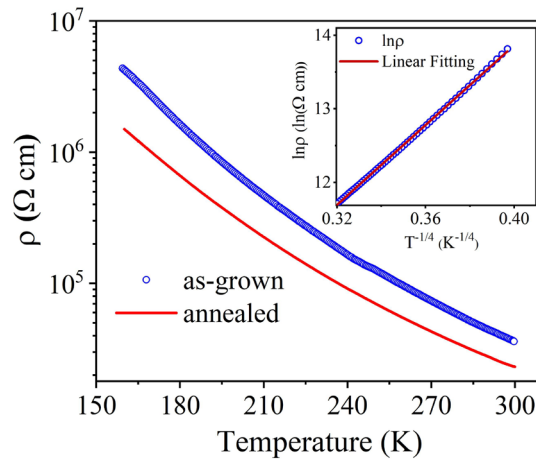


Figure 7. Electrical resistivity of polycrystals. Inset figure shows the $\ln \rho$ of as-grown sample plotted as function of $T^{-1/4}$.

In perovskite, oxygen content has a significant impact on transport properties.^{72, 73} To increase oxygen content, we annealed our pellets at 420 °C and 70 bar of oxygen for three days. **Figure 7** shows the resistivity of annealed sample (see **Figure S18** for wide range of resistivity measured by the two-probe method). It is still semiconducting, although the resistivity becomes smaller compared with as-grown samples. The resistivity of our sample is seven orders of magnitude larger compared to the LaPdO₃ tested by Penny G.⁵³ The insulating behavior of La₃Pd₂NaO₉ can be understood due to the formation of a charge-ordered pattern between Na and Pd ions. Similar phenomenon has been reported in the trilayer square planar system La₄Ni₃O₈.¹²

3.7 Magnetic susceptibility and magnetization. **Figure 8(a)** shows the magnetic susceptibility of polycrystals as a function of temperature ranging from 1.8 to 300 K. The sample exhibits paramagnetic behavior. The high-temperature magnetic susceptibility is analyzed. A Curie-Weiss fit to the ZFC-W data in the range of 200-300 K using $\chi = \chi_0 + C/(T - \theta)$, where χ_0 , C and θ are the temperature independent contribution, Curie and Weiss constants, respectively, yields $\chi_0 = 1.74 \times 10^{-5} \text{ emu mol}^{-1} \text{ Oe}^{-1}$, $C = 0.035 \text{ emu K mol}^{-1} \text{ Oe}^{-1}$ and $\theta = -269 \text{ K}$. The resulting effective moment is $0.53 \mu_B$ per Pd ion.⁷⁴ The negative value of the Weiss constant indicates antiferromagnetic interactions. According to the XPS results, the oxidation state of Pd in La₃Pd₂NaO₉ is mostly +4 with a small amount of +2. In the octahedral field, the d orbital splits into three t_{2g} orbitals and two e_g orbitals, and Pd⁴⁺ likely possess the t_{2g}^6 electronic configuration, thus it is expected to be diamagnetic. Meanwhile, Pd²⁺ has a d^8 electron configuration, similar to Ni²⁺, and may exist in two spin states: low-spin ($S = 0$) and high-spin ($S = 1$).⁵ Therefore, the observed paramagnetism may be attributed to the presence of a small fraction of high-spin Pd²⁺ caused by oxygen defects in the sample. Similar phenomena have been reported in K₂PdO₃,⁷⁵ Zn₂PdO₄,⁷⁶ KPd₂O₃,⁷⁷ and BiPd₂O₄,⁷⁸ and in these cases defects were proposed to be the reason for paramagnetism.

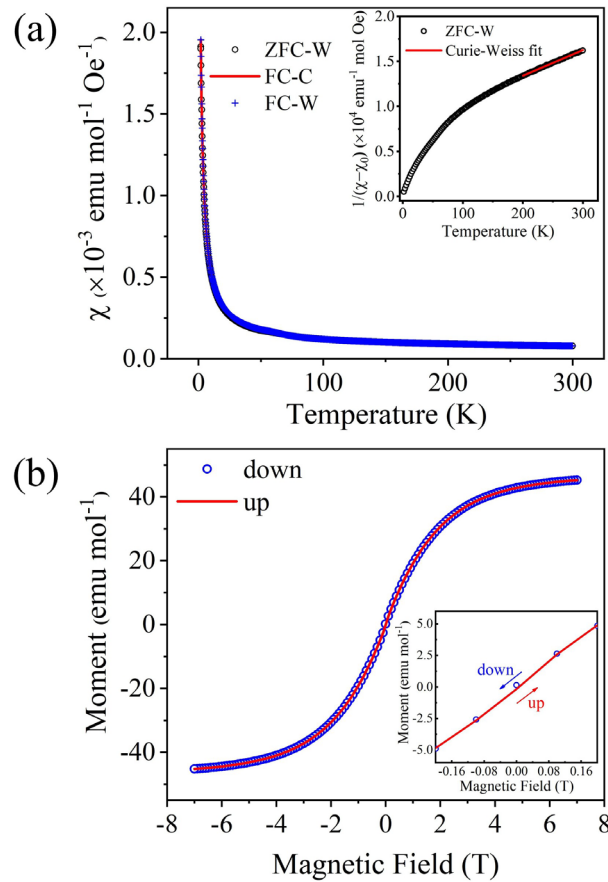


Figure 8. (a) Magnetic susceptibility of La₃Pd₂NaO₉. Inset figure shows the Curie-Weiss fit of ZFC-W. (b) Magnetization at 1.8 K as a function of magnetic fields (blue: +7 to -7 T, red: -7 to +7 T).

Figure 8(b) shows the magnetization of polycrystals at 1.8 K as a function of magnetic fields ranging from 7 T to -7 T. Magnetization as a function of magnetic fields ranging from 7 T to -7 T at 150 K and 300 K are shown in **Figure S19**. At low field, paramagnetic behavior is observed. In contrast, diamagnetic signal is clearly seen at high magnetic field, consistent with the expected $S = 0$ (t_{2g}^6 configuration) of Pd^{4+} . Considering that sodium exists in our samples and ground powders might absorb moisture, thus affecting the magnetic properties, we also measured the as-grown single crystals. The magnetic results were consistent with those of the powders, and the difference in fitting parameters are relatively small (**Figure S20**).

4. Conclusions

We have successfully grown single crystals of a high-valent palladate $\text{La}_3\text{Pd}_2\text{NaO}_9$ with dimensions of up to 20 μm on the edge at 420 $^\circ\text{C}$ and 70 bar oxygen pressure using the NaOH-KOH (molar ratio 1:1) flux system. The as-grown crystals exhibit shiny natural facets determined by its crystal symmetry. EDS, ICP and XPS measurements revealed that the chemical formula of the as-grown single crystals is $\text{La}_3\text{Pd}_2\text{NaO}_{9-\delta}$ ($\delta = 0.45$). Synchrotron X-ray single-crystal diffraction data reveals that the crystal belongs to the monoclinic $P2_1/c$ with lattice parameters of $a = 16.777(5)$ \AA , $b = 5.8311(17)$ \AA , $c = 9.759(3)$ \AA , and $\beta = 124.969(3)^\circ$. STEM measurements demonstrate excellent sample homogeneity. Resistivity measurements of $\text{La}_3\text{Pd}_2\text{NaO}_9$ indicate that it is an insulator, which can be attributed to charge ordering induced by the ordered Na and Pd. The magnetic susceptibility and magnetization data show a paramagnetic behavior, which is inconsistent with the expected t_{2g}^6 configuration ($S = 0$) for Pd^{4+} . The anomalous magnetic properties may be due to the presence of a small fraction of high-spin Pd^{2+} caused by oxygen defects in the sample. The successful preparation of $\text{La}_3\text{Pd}_2\text{NaO}_9$ single crystals with a high-valent Pd oxidation state at a relatively low temperature and oxygen pressure provides us with a new approach to explore the preparation of new R-P palladates.

Associated content

Supporting Information. The Supporting Information is available free of charge at XXX.

Tables of synthesis and growth conditions of single crystals, EDS, ICP, Rietveld refinement; and figures of powder diffraction data, LeBail fit, EDS raw data, XPS full spectrum, Rietveld refinements using various models, the reconstructed ($0kl$) and ($hk0$) planes, HAADF-STEM, electrical resistivity, and magnetic properties of as-grown crystals (PDF)

Accession Codes

CCDC 2445228 contains the supplementary crystallographic data for this paper. These data can be obtained free of charge via www.ccdc.cam.ac.uk/data_request/cif, or by emailing data_request@ccdc.cam.ac.uk, or by contacting The Cambridge Crystallographic Data Centre, 12 Union Road, Cambridge CB2 1EZ, UK; fac: +44 1223 336033

Author Information

Corresponding Author

Junjie Zhang – Institute of Crystal Materials, State Key Laboratory of Crystal Materials, Shandong University, Jinan 250100, Shandong, China; orcid.org/0000-0002-5561-1330; Email: junjie@sdu.edu.cn

Authors

Qingqing Yang – Institute of Crystal Materials, State Key Laboratory of Crystal Materials, Shandong University, Jinan 250100, Shandong, China

Ning Guo – CAS Key Laboratory of Standardization and Measurement for Nanotechnology, CAS Center for Excellence in Nanoscience, National Center for Nanoscience and Technology, Beijing 100190, China

Tieyan Chang – NSF's ChemMatCARS, The University of Chicago, Argonne, IL 60439, USA;

orcid.org/0000-0002-7434-3714

Zheng Guo – Institute of Crystal Materials, State Key Laboratory of Crystal Materials, Shandong University, Jinan 250100, Shandong, China

Xiaoli Wang – Institute of Crystal Materials, State Key Laboratory of Crystal Materials, Shandong University, Jinan 250100, Shandong, China

Chuanyan Fan – Institute of Crystal Materials, State Key Laboratory of Crystal Materials, Shandong University, Jinan 250100, Shandong, China

Chao Liu – Institute of Crystal Materials, State Key Laboratory of Crystal Materials, Shandong University, Jinan 250100, Shandong, China

Lu Han – Institute of Crystal Materials, State Key Laboratory of Crystal Materials, Shandong University, Jinan 250100, Shandong, China

Feiyu Li – Institute of Crystal Materials, State Key Laboratory of Crystal Materials, Shandong University, Jinan 250100, Shandong, China

Tao He – Institute of Crystal Materials, State Key Laboratory of Crystal Materials, Shandong University, Jinan 250100, Shandong, China

Qiang Zheng – CAS Key Laboratory of Standardization and Measurement for Nanotechnology, CAS Center for Excellence in Nanoscience, National Center for Nanoscience and Technology, Beijing 100190, China

Yu-Sheng Chen – NSF's ChemMatCARS, The University of Chicago, Argonne, IL 60439, USA

Author Contributions

The manuscript was written through the contributions of all authors.

Notes

The authors declare no competing financial interest.

Acknowledgments

Work at Shandong University was supported by the National Natural Science Foundation of China (Grant Nos. 12374457 and 12074219). J. Z. thanks Prof. Xutang Tao from Shandong University for providing valuable support and fruitful discussions. J. Z. and Q. Y. would like to acknowledge the technical support from Shandong University Core Facilities Sharing Platform. J. Z. and Q. Y. thank Menghui Chu for his help with Inductively Coupled Plasma Mass Spectroscopy, and Jiahui Lu for her help with Scanning Electron Microscopy and Energy Dispersive Spectroscopy.

References

- (1) Bednorz, J. G.; Müller, K. A. Possible high T_c superconductivity in the Ba-La-Cu-O system. *Z. Phys. B: Condens. Matter* **1986**, *64* (2), 189-193.
- (2) Keimer, B.; Kivelson, S. A.; Norman, M. R.; Uchida, S.; Zaanen, J. From quantum matter to high-temperature superconductivity in copper oxides. *Nature* **2015**, *518* (7538), 179-186.
- (3) Sanders, S. 125 questions: Exploration and Discovery; *Science*, 2021, 23.
- (4) Gui, X.; Lv, B.; Xie, W. Chemistry in Superconductors. *Chem. Rev.* **2021**, *121* (5), 2966-2991.
- (5) Nomura, Y.; Arita, R. Superconductivity in infinite-layer nickelates. *Rep. Prog. Phys.* **2022**, *85* (5), 052501.
- (6) Norman, M. R. Materials design for new superconductors. *Rep. Prog. Phys.* **2016**, *79* (7), 074502.
- (7) Tranquada, J. M.; Buttrey, D. J.; Sachan, V.; Lorenzo, J. E. Simultaneous Ordering of Holes and Spins in $\text{La}_2\text{NiO}_{4.125}$. *Phys. Rev. Lett.* **1994**, *73* (7), 1003-1006.
- (8) Chaloupka, J.; Khaliullin, G. Orbital Order and Possible Superconductivity in $\text{LaNiO}_3/\text{LaMO}_3$ Superlattices. *Phys. Rev. Lett.* **2008**, *100* (1), 016404.

- (9) Poltavets, V. V.; Lokshin, K. A.; Nevidomskyy, A. H.; Croft, M.; Tyson, T. A.; Hadermann, J.; Van Tendeloo, G.; Egami, T.; Kotliar, G.; ApRoberts-Warren, N.; Dioguardi, A. P.; Curro, N. J.; Greenblatt, M. Bulk Magnetic Order in a Two-Dimensional $\text{Ni}^{1+}/\text{Ni}^{2+}$ (d^9/d^8) Nickelate, Isoelectronic with Superconducting Cuprates. *Phys. Rev. Lett.* **2010**, *104* (20), 206403.
- (10) Uchida, M.; Ishizaka, K.; Hansmann, P.; Kaneko, Y.; Ishida, Y.; Yang, X.; Kumai, R.; Toschi, A.; Onose, Y.; Arita, R.; Held, K.; Andersen, O. K.; Shin, S.; Tokura, Y. Pseudogap of Metallic Layered Nickelate $\text{R}_{2-x}\text{Sr}_x\text{NiO}_4$ ($\text{R} = \text{Nd}, \text{Eu}$) Crystals Measured Using Angle-Resolved Photoemission Spectroscopy. *Phys. Rev. Lett.* **2011**, *106* (2), 027001.
- (11) Ulbrich, H.; Braden, M. Neutron scattering studies on stripe phases in non-cuprate materials. *Phys. C (Amsterdam, Neth.)* **2012**, *481*, 31-45.
- (12) Zhang, J.; Chen, Y. S.; Phelan, D.; Zheng, H.; Norman, M. R.; Mitchell, J. F. Stacked charge stripes in the quasi-2D trilayer nickelate $\text{La}_4\text{Ni}_3\text{O}_8$. *Proc. Natl. Acad. Sci. U.S.A.* **2016**, *113* (32), 8945-8950.
- (13) Zhang, J.; Botana, A. S.; Freeland, J. W.; Phelan, D.; Zheng, H.; Pardo, V.; Norman, M. R.; Mitchell, J. F. Large orbital polarization in a metallic square-planar nickelate. *Nat. Phys.* **2017**, *13* (9), 864-869.
- (14) Li, D.; Lee, K.; Wang, B. Y.; Osada, M.; Crossley, S.; Lee, H. R.; Cui, Y.; Hikita, Y.; Hwang, H. Y. Superconductivity in an infinite-layer nickelate. *Nature* **2019**, *572* (7771), 624-627.
- (15) Osada, M.; Wang, B. Y.; Lee, K.; Li, D.; Hwang, H. Y. Phase diagram of infinite layer praseodymium nickelate $\text{Pr}_{1-x}\text{Sr}_x\text{NiO}_2$ thin films. *Phys. Rev. Mater.* **2020**, *4* (12), 121801.
- (16) Pan, G. A.; Ferenc Segedin, D.; LaBollita, H.; Song, Q.; Nica, E. M.; Goodge, B. H.; Pierce, A. T.; Doyle, S.; Novakov, S.; Córdoba Carrizales, D.; N'Diaye, A. T.; Shafer, P.; Paik, H.; Heron, J. T.; Mason, J. A.; Yacoby, A.; Kourkoutis, L. F.; Erten, O.; Brooks, C. M.; Botana, A. S.; Mundy, J. A. Superconductivity in a quintuple-layer square-planar nickelate. *Nat. Mater.* **2022**, *21* (2), 160-164.
- (17) Wang, N. N.; Yang, M. W.; Yang, Z.; Chen, K. Y.; Zhang, H.; Zhang, Q. H.; Zhu, Z. H.; Uwatoko, Y.; Gu, L.; Dong, X. L.; Sun, J. P.; Jin, K. J.; Cheng, J. G. Pressure-induced monotonic enhancement of T_c to over 30 K in superconducting $\text{Pr}_{0.82}\text{Sr}_{0.18}\text{NiO}_2$ thin films. *Nat. Commun.* **2022**, *13* (1), 4367.
- (18) Zeng, S.; Li, C.; Er Chow, L.; Cao, Y.; Zhang, Z.; Tang, C. S.; Yin, X.; Lim, Z. S.; Hu, J.; Yang, P.; Ariando, A. Superconductivity in infinite-layer nickelate $\text{La}_{1-x}\text{Ca}_x\text{NiO}_2$ thin films. *Sci. Adv.* **2022**, *8* (7), eabl9927.
- (19) Chow, S. L. E.; Luo, Z.; Ariando, A. Bulk superconductivity near 40 K in hole-doped SmNiO_2 at ambient pressure. *Nature* **2025**, *642* (8066), 58-63.
- (20) Sun, H.; Huo, M.; Hu, X.; Li, J.; Liu, Z.; Han, Y.; Tang, L.; Mao, Z.; Yang, P.; Wang, B.; Cheng, J.; Yao, D.-X.; Zhang, G.-M.; Wang, M. Signatures of superconductivity near 80 K in a nickelate under high pressure. *Nature* **2023**, *621* (7979), 493-498.
- (21) Hou, J.; Yang, P.-T.; Liu, Z.-Y.; Li, J.-Y.; Shan, P.-F.; Ma, L.; Wang, G.; Wang, N.-N.; Guo, H.-Z.; Sun, J.-P.; Uwatoko, Y.; Wang, M.; Zhang, G.-M.; Wang, B.-S.; Cheng, J.-G. Emergence of High-Temperature Superconducting Phase in Pressurized $\text{La}_3\text{Ni}_2\text{O}_7$ Crystals. *Chin. Phys. Lett.* **2023**, *40* (11), 117302.
- (22) Zhang, Y.; Su, D.; Huang, Y.; Shan, Z.; Sun, H.; Huo, M.; Ye, K.; Zhang, J.; Yang, Z.; Xu, Y.; Su, Y.; Li, R.; Smidman, M.; Wang, M.; Jiao, L.; Yuan, H. High-temperature superconductivity with zero resistance and strange-metal behaviour in $\text{La}_3\text{Ni}_2\text{O}_{7-\delta}$. *Nat. Phys.* **2024**, *20* (8), 1269-1273.
- (23) Li, Q.; Zhang, Y.-J.; Xiang, Z.-N.; Zhang, Y.; Zhu, X.; Wen, H.-H. Signature of Superconductivity in Pressurized $\text{La}_4\text{Ni}_3\text{O}_{10}$. *Chin. Phys. Lett.* **2024**, *41* (1), 017401.
- (24) Zhu, Y.; Peng, D.; Zhang, E.; Pan, B.; Chen, X.; Chen, L.; Ren, H.; Liu, F.; Hao, Y.; Li, N.; Xing, Z.; Lan, F.; Han, J.; Wang, J.; Jia, D.; Wo, H.; Gu, Y.; Gu, Y.; Ji, L.; Wang, W.; Gou, H.; Shen, Y.; Ying, T.; Chen, X.; Yang, W.; Cao, H.; Zheng, C.; Zeng, Q.; Guo, J.-g.; Zhao, J. Superconductivity in pressurized trilayer $\text{La}_4\text{Ni}_3\text{O}_{10-\delta}$ single crystals. *Nature* **2024**, *631* (8021), 531-536.
- (25) Chen, X.; Poldi, E. H. T.; Huyan, S.; Chapai, R.; Zheng, H.; Bud'ko, S. L.; Welp, U.; Canfield, P. C.; Hemley, R. J.; Mitchell, J. F.; Phelan, D. Low fractional volume superconductivity in single crystals of $\text{Pr}_4\text{Ni}_3\text{O}_{10}$ under pressure. *Phys. Rev. B* **2025**, *111* (9), 094525.

- (26) Zhang, M.; Pei, C.; Peng, D.; Du, X.; Hu, W.; Cao, Y.; Wang, Q.; Wu, J.; Li, Y.; Liu, H.; Wen, C.; Song, J.; Zhao, Y.; Li, C.; Cao, W.; Zhu, S.; Zhang, Q.; Yu, N.; Cheng, P.; Zhang, L.; Li, Z.; Zhao, J.; Chen, Y.; Jin, C.; Guo, H.; Wu, C.; Yang, F.; Zeng, Q.; Yan, S.; Yang, L.; Qi, Y. Superconductivity in trilayer nickelate $\text{La}_4\text{Ni}_3\text{O}_{10}$ under pressure. *Phys. Rev. X* **2025**, *15* (2), 021005.
- (27) Zhang, E.; Peng, D.; Zhu, Y.; Chen, L.; Cui, B.; Wang, X.; Wang, W.; Zeng, Q.; Zhao, J. Bulk Superconductivity in Pressurized Trilayer Nickelate $\text{Pr}_4\text{Ni}_3\text{O}_{10}$ Single Crystals. *Phys. Rev. X* **2025**, *15* (2), 021008.
- (28) Li, F.; Guo, N.; Zheng, Q.; Shen, Y.; Wang, S.; Cui, Q.; Liu, C.; Wang, S.; Tao, X.; Zhang, G.-M.; Zhang, J. Design and synthesis of three-dimensional hybrid Ruddlesden-Popper nickelate single crystals. *Phys. Rev. Mater.* **2024**, *8* (5), 053401.
- (29) Chen, X.; Zhang, J.; Thind, A. S.; Sharma, S.; LaBollita, H.; Peterson, G.; Zheng, H.; Phelan, D. P.; Botana, A. S.; Klie, R. F.; Mitchell, J. F. Polymorphism in the Ruddlesden-Popper Nickelate $\text{La}_3\text{Ni}_2\text{O}_7$: Discovery of a Hidden Phase with Distinctive Layer Stacking. *J. Am. Chem. Soc.* **2024**, *146* (6), 3640-3645.
- (30) Wang, H.; Chen, L.; Rutherford, A.; Zhou, H.; Xie, W. Long-Range Structural Order in a Hidden Phase of Ruddlesden-Popper Bilayer Nickelate $\text{La}_3\text{Ni}_2\text{O}_7$. *Inorg. Chem.* **2024**, *63* (11), 5020-5026.
- (31) Puphal, P.; Reiss, P.; Enderlein, N.; Wu, Y. M.; Khaliullin, G.; Sundaramurthy, V.; Priessnitz, T.; Knauff, M.; Suthar, A.; Richter, L.; Isobe, M.; Van Aken, P. A.; Takagi, H.; Keimer, B.; Suyolcu, Y. E.; Wehinger, B.; Hansmann, P.; Hepting, M. Unconventional crystal structure of the high-pressure superconductor $\text{La}_3\text{Ni}_2\text{O}_7$. *Phys. Rev. Lett.* **2024**, *133* (14), 146002.
- (32) Shi, M.; Peng, D.; Fan, K.; Xing, Z.; Yang, S.; Wang, Y.; Li, H.; Wu, R.; Du, M.; Ge, B.; Zeng, Z.; Zeng, Q.; Ying, J.; Wu, T.; Chen, X. Superconductivity of the hybrid Ruddlesden-Popper $\text{La}_5\text{Ni}_3\text{O}_{11}$ single crystals under high pressure, arXiv: 2502.01018. arXiv.org e-Print archive. <https://arxiv.org/abs/2502.01018> (accessed 2025-06-11).
- (33) Ko, E. K.; Yu, Y.; Liu, Y.; Bhatt, L.; Li, J.; Thampy, V.; Kuo, C.-T.; Wang, B. Y.; Lee, Y.; Lee, K.; Lee, J.-S.; Goodge, B. H.; Muller, D. A.; Hwang, H. Y. Signatures of ambient pressure superconductivity in thin film $\text{La}_3\text{Ni}_2\text{O}_7$. *Nature* **2025**, *638* (8052), 935-940.
- (34) Zhou, G.; Lv, W.; Wang, H.; Nie, Z.; Chen, Y.; Li, Y.; Huang, H.; Chen, W.-Q.; Sun, Y.-J.; Xue, Q.-K.; Chen, Z. Ambient-pressure superconductivity onset above 40 K in $(\text{La,Pr})_3\text{Ni}_2\text{O}_7$ films. *Nature* **2025**, *640* (8059), 641-646.
- (35) Li, F.; Xing, Z.; Peng, D.; Dou, J.; Guo, N.; Ma, L.; Zhang, Y.; Wang, L.; Luo, J.; Yang, J.; Zhang, J.; Chang, T.; Chen, Y.-S.; Cai, W.; Cheng, J.; Wang, Y.; Zeng, Z.; Zheng, Q.; Zhou, R.; Zeng, Q.; Tao, X.; Zhang, J. Ambient pressure growth of bilayer nickelate single crystals with superconductivity over 90 K under high pressure, arXiv: 2501.14584v2. arXiv.org e-Print archive. <https://arxiv.org/abs/2501.14584v2> (accessed 2025-06-11).
- (36) Botana, A. S.; Norman, M. R. Layered palladates and their relation to nickelates and cuprates. *Phys. Rev. Mater.* **2018**, *2* (10), 104803.
- (37) Hirayama, M.; Tadano, T.; Nomura, Y.; Arita, R. Materials design of dynamically stable d^9 layered nickelates. *Phys. Rev. B* **2020**, *101* (7), 075107.
- (38) Kitatani, M.; Si, L.; Janson, O.; Arita, R.; Zhong, Z.; Held, K. Nickelate superconductors—a renaissance of the one-band Hubbard model. *npj Quantum Mater.* **2020**, *5* (1), 59.
- (39) Held, K.; Si, L.; Worm, P.; Janson, O.; Arita, R.; Zhong, Z.; Tomczak, J. M.; Kitatani, M. Phase Diagram of Nickelate Superconductors Calculated by Dynamical Vertex Approximation. *Front. Phys.* **2022**, *9*, 810394.
- (40) Kitatani, M.; Si, L.; Worm, P.; Tomczak, J. M.; Arita, R.; Held, K. Optimizing Superconductivity: From Cuprates via Nickelates to Palladates. *Phys. Rev. Lett.* **2023**, *13* (16), 166002.
- (41) Kitamine, N.; Ochi, M.; Kuroki, K. Theoretical designing of multiband Nickelate and Palladate superconductors with $d^{8+\delta}$ configuration, arXiv: 2308.12750. arXiv.org e-Print archive. <https://arxiv.org/abs/2308.12750> (accessed 2025-06-11).
- (42) Pickett, W. E. Electronic structure of the high-temperature oxide superconductors. *Rev. Mod. Phys.* **1989**, *61* (2), 433-512.
- (43) Harada, T.; Sugawara, K.; Fujiwara, K.; Kitamura, M.; Ito, S.; Nojima, T.; Horiba, K.; Kumigashira, H.; Takahashi,

- T.; Sato, T.; Tsukazaki, A. Anomalous Hall effect at the spontaneously electron-doped polar surface of PdCoO₂ ultrathin films. *Phys. Rev. Res.* **2020**, *2* (1), 013282.
- (44) Wen, C.; Qin, T.; Zhang, X.; Zhang, M.; Hu, W.; Shen, S.; Yang, Z.; Qi, Y.; Li, G.; Yan, S. Probing Hidden Mott Gap and Incommensurate Charge Modulation on the Polar Surfaces of PdCrO₂. *Phys. Rev. Lett.* **2023**, *131* (11), 116501.
- (45) Kushwaha, P.; Borrmann, H.; Khim, S.; Rosner, H.; Moll, P. J. W.; Sokolov, D. A.; Sunko, V.; Grin, Y.; Mackenzie, A. P. Single Crystal Growth, Structure, and Electronic Properties of Metallic Delafossite PdRhO₂. *Cryst. Growth Des.* **2017**, *17* (8), 4144-4150.
- (46) Zhang, J.; Tao, X. Review on quasi-2D square planar nickelates. *CrystEngComm* **2021**, *23* (18), 3249-3264.
- (47) Tsujimoto, Y.; Tassel, C.; Hayashi, N.; Watanabe, T.; Kageyama, H.; Yoshimura, K.; Takano, M.; Ceretti, M.; Ritter, C.; Paulus, W. Infinite-layer iron oxide with a square-planar coordination. *Nature* **2007**, *450* (7172), 1062-1065.
- (48) Shibasaki, S.; Terasaki, I. Thermoelectric Properties of Layered Pd Oxide R₂PdO₄ (R = La, Nd, Sm, and Gd). *J. Phys. Soc. Jpn.* **2006**, *75* (2), 024705.
- (49) Kim, S.-J.; Lemaux, S.; Demazeau, G.; Kim, J.-Y.; Choy, J.-H. LaPdO₃: The First Pd^{III} Oxide with the Perovskite Structure. *J. Am. Chem. Soc.* **2001**, *123* (42), 10413-10414.
- (50) Attfield, J. P.; Férey, G. Structural correlations within the lanthanum palladium oxide family. *J. Solid State Chem.* **1989**, *80* (2), 286-298.
- (51) Suzuki, S.; Kawashima, K.; Ito, W.; Igarashi, S.; Yoshikawa, M.; Akimitsu, J. Transport and Magnetic Properties of Ln_{2-x}Ce_xPdO₄ (Ln = Nd, Sm, and Eu) with the PdO₂ Layer. In Proceedings of the International Conference on Strongly Correlated Electron Systems (SCES2013), 2014, 017028.
- (52) Nanao, Y.; Krockenberger, Y.; Ikeda, A.; Taniyasu, Y.; Naito, M.; Yamamoto, H. Crystal growth and metal-insulator transition in two-dimensional layered rare-earth palladates. *Phys. Rev. Mater.* **2018**, *2* (8), 085003.
- (53) Penny, G. B. S. High-pressure synthesis of electronic materials. Ph.D. Thesis, University of Edinburgh, Edinburgh, U.K., 2010.
- (54) Jacob, K. T.; Lwin, K. T.; Waseda, Y. System La-Pd-O: phase diagram and thermodynamic properties of ternary oxides. *Solid State Sci.* **2002**, *4* (2), 205-215.
- (55) Bruker. *Computer code APEX4*; Bruker Analytical X-ray Instruments, Bruker Inc.: Madison, Wisconsin, USA, 2022.
- (56) Rakshit, S.; Gopalakrishnan, P. S. Oxygen nonstoichiometry and its effect on the structure of LaNiO₃. *J. Solid State Chem.* **1994**, *110* (1), 28-31.
- (57) Shivakumara, C.; Hegde, M. S.; Prakash, A. S.; Khadar, A. M. A.; Subbanna, G. N.; Lalla, N. P. Low temperature synthesis, structure and properties of alkali-doped La₂NiO₄, LaNiO₃ and LaNi_{0.85}Cu_{0.15}O₃ from alkali hydroxide fluxes. *Solid State Sci.* **2003**, *5* (2), 351-357.
- (58) Azuma, M.; Saito, T.; Ishiwata, S.; Yamada, I.; Kohsaka, Y.; Takagi, H.; Takano, M. Single crystal growth of transition metal oxides at high pressures of several GPa. *Phys. C (Amsterdam, Neth.)* **2003**, *392* (1), 22-28.
- (59) Alonso, J. A.; Muñoz, A.; Largeteau, A.; Demazeau, G. Crystal growth of NdNiO₃ perovskite under high oxygen pressure. *J. Phys.: Condens. Matter* **2004**, *16* (14), S1277-S1281.
- (60) Klein, Y. M.; Kozłowski, M.; Linden, A.; Lacorre, P.; Medarde, M.; Gawryluk, D. J. RENiO₃ Single Crystals (RE = Nd, Sm, Gd, Dy, Y, Ho, Er, Lu) Grown from Molten Salts under 2000 bar of Oxygen Gas Pressure. *Cryst. Growth Des.* **2021**, *21* (7), 4230-4241.
- (61) Li, F.; Wang, S.; Ma, C.; Wang, X.; Liu, C.; Fan, C.; Han, L.; Wang, S.; Tao, X.; Zhang, J. Flux Growth of Trilayer La₄Ni₃O₁₀ Single Crystals at Ambient Pressure. *Cryst. Growth Des.* **2023**, *24* (1), 347-354.
- (62) Mugavero, S. J.; Gemmill, W. R.; Roof, I. P.; zur Loye, H.-C. Materials discovery by crystal growth: Lanthanide metal containing oxides of the platinum group metals (Ru, Os, Ir, Rh, Pd, Pt) from molten alkali metal hydroxides. *J. Solid State Chem.* **2009**, *182* (7), 1950-1963.
- (63) Smallwood, P. L.; Smith, M. D.; zur Loye, H.-C. Flux synthesis of alkaline earth palladates. *J. Cryst. Growth* **2000**,

216 (1-4), 299-303.

- (64) Mugavero, S. J.; Smith, M. D.; zur Loye, H.-C. Crystal Growth and Structural Characterization of the New Ordered Palladates LnKPdO_3 ($\text{Ln} = \text{La}, \text{Pr}, \text{Nd}, \text{Sm}-\text{Gd}$) and the Isostructural, Partially Cu-Substituted Palladate $\text{PrK}(\text{Cu}_{0.14}\text{Pd}_{0.86})\text{O}_3$. *Inorg. Chem.* **2007**, *46* (8), 3116-3122.
- (65) Mugavero Iii, S. J.; Smith, M. D.; zur Loye, H.-C. Crystal Growth and Structural Characterization of a New Series of Rare Earth Palladates, $\text{LnNaPd}_6\text{O}_8$ ($\text{Ln} = \text{Tb} - \text{Lu}, \text{Y}$). *Cryst. Growth Des.* **2008**, *8* (2), 494-500.
- (66) Wang, X.; Wang, S.; Liu, C.; Fan, C.; Han, L.; Li, F.; Chang, T.; Chen, Y.-S.; Wang, S.; Tao, X.; Zhang, J. High pO_2 Flux Growth and Characterization of NdNiO_3 Crystals. *Crystals* **2023**, *13* (2), 180.
- (67) Lupan, O.; Postica, V.; Hoppe, M.; Wolff, N.; Polonskyi, O.; Pauporté, T.; Viana, B.; Majérus, O.; Kienle, L.; Faupel, F.; Adelung, R. PdO/PdO₂ functionalized ZnO: Pd films for lower operating temperature H₂ gas sensing. *Nanoscale* **2018**, *10* (29), 14107-14127.
- (68) Mucalo, M.; Bullen, C. Electric arc generated (Bredig) palladium nanoparticles: Surface analysis by X-ray photoelectron spectroscopy for samples prepared at different pH. *J. Mater. Sci. Lett.* **2001**, *20* (20), 1853-1856.
- (69) Domashevskaya, E.; Ryabtsev, S.; Turishchev, S. Y.; Kashkarov, V.; Yurakov, Y. A.; Chuvenkova, O.; Shchukarev, A. V. XPS and XANES studies of SnO_x nanolayers. *J. Struct. Chem.* **2008**, *49*, 80-91.
- (70) Kibis, L.; Titkov, A.; Stadnichenko, A.; Koscheev, S.; Boronin, A. X-ray photoelectron spectroscopy study of Pd oxidation by RF discharge in oxygen. *Appl. Surf. Sci.* **2009**, *255* (22), 9248-9254.
- (71) Mott, N. F.; Davis, E. A. *Electronic processes in non-crystalline materials*; New York, Clarendon Press, 1979.
- (72) Taniguchi, S.; Nishikawa, T.; Yasui, Y.; Kobayashi, Y.; Takeda, J.; Shamoto, S. i.; Sato, M. Transport, Magnetic and Thermal Properties of $\text{La}_3\text{Ni}_2\text{O}_{7-\sigma}$. *J. Phys. Soc. Jpn.* **1995**, *64* (5), 1644-1650.
- (73) Carvalho, M. D.; Cruz, M. M.; Wattiaux, A.; Bassat, J. M.; Costa, F. M. A.; Godinho, M. Influence of oxygen stoichiometry on the electronic properties of $\text{La}_4\text{Ni}_3\text{O}_{10\pm\delta}$. *J. Appl. Phys.* **2000**, *88* (1), 544-549.
- (74) Mugiraneza, S.; Hallas, A. M. Tutorial: a beginner's guide to interpreting magnetic susceptibility data with the Curie-Weiss law. *Commun. Phys.* **2022**, *5* (1), 95.
- (75) Wilhelm, M.; Hoppe, R. Zur Kenntnis der Oxopalladate der Alkalimetalle [1]. *Z. Anorg. Allg. Chem.* **1976**, *424* (1), 5-12.
- (76) Demazeau, G.; Omeran, I.; Pouchard, M.; Hagenmuller, P. Sur une nouvelle phase oxygenee du palladium +IV: Zn_2PdO_4 . *Mater. Res. Bull.* **1976**, *11* (11), 1449-1452.
- (77) Panin, R. V.; Khasanova, N. R.; Bougerol, C.; Schnelle, W.; Van Tendeloo, G.; Antipov, E. V. Ordering of Pd^{2+} and Pd^{4+} in the Mixed-Valent Palladate KPd_2O_3 . *Inorg. Chem.* **2010**, *49* (4), 1295-1297.
- (78) Yi, W.; Matsushita, Y.; Tanaka, M.; Belik, A. A. High-Pressure Synthesis, Crystal Structure, and Properties of BiPd_2O_4 with Pd^{2+} and Pd^{4+} Ordering and PbPd_2O_4 . *Inorg. Chem.* **2012**, *51* (14), 7650-7656.

For Table of Contents Only

